Paradoxical glomerular filtration of carbon nanotubes

Alessandro Ruggiero[a], Carlos H. Villa[a], Evan Bander[a], Diego A. Rey[b], Magnus Bergkvist[c], Carl A. Batt[d], Katia Manova-Todorova[a], William M. Deen[e], David A. Scheinberg[a,1], and Michael R. McDevitt[a,1]

[a]Departments of Medicine, Radiology, Molecular Pharmacology and Chemistry or the Molecular Cytology Core Facility, Memorial Sloan-Kettering Cancer Center, New York, NY 10065; Departments of [b]Biomedical Engineering and [d]Food Science, Cornell University, Ithaca, NY 14853; [c]College of Nanoscale Science and Engineering, University at Albany, Albany, NY 12203; and [e]Department of Chemical Engineering, Massachusetts Institute of Technology, Cambridge, MA 02139

Edited by Sheldon Weinbaum, City College of New York, New York, NY, and approved May 25, 2010 (received for review November 25, 2009)

The molecular weight cutoff for glomerular filtration is thought to be 30–50 kDa. Here we report rapid and efficient filtration of molecules 10–20 times that mass and a model for the mechanism of this filtration. We conducted multimodal imaging studies in mice to investigate renal clearance of a single-walled carbon nanotube (SWCNT) construct covalently appended with ligands allowing simultaneous dynamic positron emission tomography, near-infrared fluorescence imaging, and microscopy. These SWCNTs have a length distribution ranging from 100 to 500 nm. The average length was determined to be 200–300 nm, which would yield a functionalized construct with a molecular weight of ∼350–500 kDa. The construct was rapidly ($t_{1/2}$ ∼ 6 min) renally cleared intact by glomerular filtration, with partial tubular reabsorption and transient translocation into the proximal tubular cell nuclei. Directional absorption was confirmed in vitro using polarized renal cells. Active secretion via transporters was not involved. Mathematical modeling of the rotational diffusivity showed the tendency of flow to orient SWCNTs of this size to allow clearance via the glomerular pores. Surprisingly, these results raise questions about the rules for renal filtration, given that these large molecules (with aspect ratios ranging from 100:1 to 500:1) were cleared similarly to small molecules. SWCNTs and other novel nanomaterials are being actively investigated for potential biomedical applications, and these observations—that high aspect ratio as well as large molecular size have an impact on glomerular filtration—will allow the design of novel nanoscale-based therapeutics with unusual pharmacologic characteristics.

multimodal imaging | nanotechnology | renal

Carbon nanotubes (CNTs) have interesting properties and have been proposed as novel components of drugs and devices in pharmaceutical and biomedical applications (1). CNTs have unique intrinsic physical, chemical, electronic, thermal, and optical properties and can be chemically modified (with, e.g., targeting ligands, magnetic, radioactive, fluorescent, and chemotherapeutic moieties) to exhibit additional extrinsic properties (2–4). Pharmacokinetic (PK) studies of covalently functionalized single-wall CNTs (SWCNTs) (5–9) and multiwall (MWCNTs) (10–12) have reported a short blood compartment half-life (1–3 h) and limited tissue (kidneys, liver, and spleen) accumulation and renal excretion. Clearance via renal mechanisms is significant (13), because it provides the opportunity for the host to eliminate SWCNTs, allowing potential therapeutic and diagnostic applications in vivo. The elimination of noncovalently modified SWCNTs has been reported to favor the hepatobiliary route, with evidence of a minor role for the renal route (14).

Renal clearance of solutes occurs through a combination of glomerular filtration, active tubular secretion, and passive tubular reabsorption (15). In previous work, we reported radioactivity in the renal cortex and in the urine within 1 h of administration of radiolabeled SWCNTs, but were unable to describe the mechanism (8). Others have documented renal filtration of MWCNTs, showing that it was possible for these high–molecular weight (MW) molecules to pass through the glomerulus (10–12). Other possible elimination processes of secretion or reabsorption have not been evaluated. Skepticism about the renal excretion of CNTs remains (16), however, given the lack of a complete biologic mechanism and of confirmation of the identity and quantity of the bulk of the excreted CNTs and its microlocalization within the kidney. Consequently, we designed a covalently functionalized SWCNT construct, suitable for several different imaging modalities, to explore the global and local PK profile in an animal model, and performed a series of experiments to investigate the net contributions of renal filtration, secretion, and reabsorption to clearance and to comment on the identity of the eliminated SWCNTs. Importantly, we explained the experimental data by mathematically modeling the rotational diffusivity of this high–aspect ratio, high-MW molecule.

In the present work, SWCNTs were covalently functionalized with amino groups, appended with two fluorescent dyes [Alexa Fluor (AF) 488 and AF680] and metal-ion chelands (DOTA), radiolabeled with ^{86}Y, and fully characterized before and after injection into mice. The PK of the resulting construct, SWCNT-[([^{86}Y]DOTA)(AF488)(AF680)], was determined through dynamic PET of the entire animal, near-infrared (NIR) fluorescence imaging of the kidney, and immunohistochemistry (IHC) and immunofluorescence (IF) imaging of the nephron, taking advantage of the different imaging modalities appended to the construct.

Results

Synthesis and Characterization of Size, Charge, and Composition of Multifunctionalized SWCNTs. The high-purity, high-pressure carbon monoxide (HiPCO)-produced SWCNTs used as starting materials have individual tube lengths of 100–1,000 nm and diameters of 0.8–1.2 nm. We did not acid-oxidize nor sonicate at high power our SWCNT material at any step. After covalent functionalization (2), the chromatographic, transmission electron microscopy (TEM), chemical, spectroscopic, and Raman characterizations were performed as described previously (7–9) and confirmed the identity, stoichiometry, and purity of the nanomaterials (Fig. 1). Through TEM analyses of our materials dried onto a substrate, we observed bundled aggregates of SWCNTs with a mean length of 195 ± 69 nm (n = 644) and lengths spanning a 500 nm range (Fig. S1). Dynamic light scattering (DLS) showed an average hydrodynamic radius of 105 ± 2.9 nm for the construct (range, 90–900 nm). Based on these DLS data (and the assumptions provided in *Discussion* and *Materials and Methods*), the average SWCNT length was calculated to be ∼300 nm (assuming a CNT rod shape with d ∼ 1 nm). A ζ-potential value of −8.9 ± 3.3 mV revealed that the construct had an overall negative charge. Therefore, both

Author contributions: A.R., D.A.S., and M.R.M. designed research; A.R., C.H.V., E.B., D.A.R., M.B., K.M.-T., W.M.D., and M.R.M. performed research; A.R., C.H.V., E.B., D.A.R., M.B., C.A.B., K.M.-T., W.M.D., and M.R.M. contributed new reagents/analytic tools; A.R., C.H.V., E.B., D.A.R., M.B., C.A.B., K.M.-T., W.M.D., D.A.S., and M.R.M. analyzed data; and A.R., W.M.D., D.A.S., and M.R.M. wrote the paper.

Conflict of interest statement: D.A.S. is a consultant for Enscyce.

This article is a PNAS Direct Submission.

[1]To whom correspondence may be addressed. E-mail: m-mcdevitt@ski.mskcc.org or d-scheinberg@ski.mskcc.org.

This article contains supporting information online at www.pnas.org/lookup/suppl/doi:10.1073/pnas.0913667107/-/DCSupplemental.

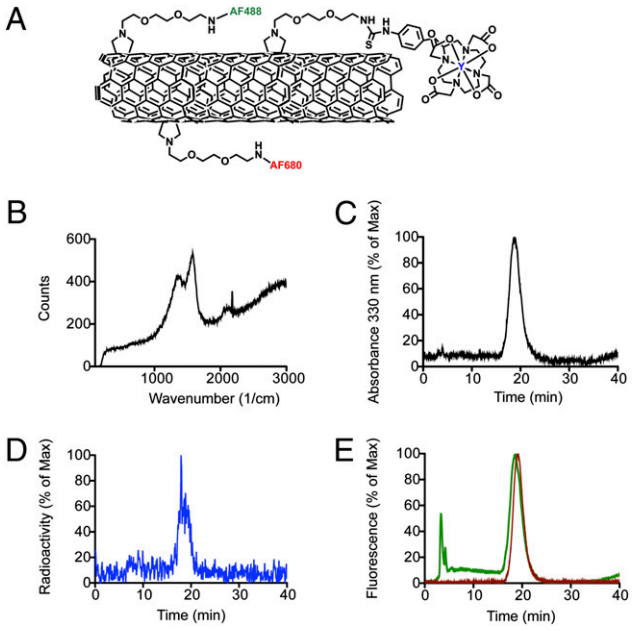

Fig. 1. Water-soluble CNT covalently functionalized with DOTA, AF488, and AF680. (*A*) Schematic representation of the key appended moieties of the SWCNT-[([^{86}Y]DOTA)(AF488)(AF680)] construct. (*B*) Raman spectrum of the purified SWCNT-NH_2 starting material. (*C*–*E*) Reverse-phase HPLC chromatographs of SWCNT-[([^{86}Y]DOTA)(AF488)(AF680)] showing a UV-Vis trace of the absorbance at 330 nm (CNT signature) (*C*), a radioactivity trace of the ^{86}Y (*D*), and superimposed fluorescence traces of the AF488 (green) and AF680 (red) dye moieties (*E*).

methods of analysis yielded a largely overlapping, polydispersed size range with an average length of 200–300 nm. The SWCNT-[(DOTA)(AF488)(AF680)] construct was assayed to contain 0.02 mmol AF488, 0.04 mmol AF680, and 0.4 mmol DOTA per gram of SWCNT. Using these values, representative constructs of L ~200–300 nm would have a MW of ~350–500 kDa and have 7–10 AF488 moieties, 14–20 AF680 moieties, and 140–200 DOTA moieties appended per molecule. Shorter and longer constructs would have proportionally smaller and larger MW. The radiolabeled SWCNT-[([^{86}Y]DOTA)(AF488)(AF680)] construct had a specific activity of 322 GBq/g (8.7 Ci/g) and was 96% radiochemically pure. Reverse-phase radio-HPLC analysis confirmed the identity of the radiolabeled product, which contained ^{86}Y activity (>95%), the characteristic CNT UV-Vis spectral signature, and both fluorophore (488 and 680 nm) absorbance and fluorescence signals (Fig. 1).

High-MW CNT Constructs Are Excreted Intact via Glomerular Filtration in the First Seconds After Injection. After injection of the construct, dynamic PET images showed rapid (<1 min) construct accumulation in the kidneys (Fig. 2 *A* and *C*). Radioactivity, measured by volume of interest (VOI), increased rapidly in the first seconds postinjection, representing mainly the renal blood pool activity, and reached a peak at ≈3 min postinjection. Radioactivity also appeared in the bladder immediately postinjection and plateaued after 20 min (Fig. 2 *B* and *D*).

We investigated the contribution of active secretion to the clearance mechanism through competitive inhibition studies. Cimetidine, probenecid, and gentamicin were administered to block the organic cation transporter (OCT), organic anion transporter (OAT), and megalin transport systems, respectively (17–19). The time–activity curve data from the kidneys (Fig. 2*C*) and bladder (Fig. 2*D*) were not statistically significantly different among the groups. Rapid blood clearance was observed as reported previously (6–11). VOI analysis of the dynamic PET images of the heart was used to yield a $t_{1/2}$ of 6–10 min for blood compartment clearance, whereas a $t_{1/2}$ of 6 min was seen for activity in the bladder to plateau. Ex vivo biodistribution at 1 h postinjection confirmed the PET data. There were no statistically significant differences in the kidney or other harvested tissue among the groups (Fig. 2*E*). Competitive inhibition of the OAT, OCT, or megalin transport systems did not affect clearance of the construct, ruling out active secretion or reabsorption via these transporters as components of renal processing and elimination.

The identity of the excreted construct was characterized by HPLC analysis of the urine samples. Chromatographs of the urine of mice that received the radiolabeled construct for PET studies contained a radio peak that eluted with the same retention time as the injected construct (Fig. 2*F*). Similarly, chromatographs of the urine of mice injected with the construct for NIR imaging, IHC, and IF studies showed a fluorescent peak that eluted with the same retention time as the injected construct (Fig. 2*G*). The intact construct was found in the urine, validating that the imaged signals were associated with the construct. Additional analyses of urine samples from mice that received 6- to 40-fold higher doses of construct showed the characteristic UV-Vis spectrum of the SWCNTs in the chromatographic peak attributed to the construct (Fig. S2). Analysis of urine samples from mice that received injections of only the hydrolyzed dyes (Fig. S3) revealed that the unattached dyes eluted earlier and at very different times compared with the urine samples containing the intact construct.

SWCNTs Are Partially Reabsorbed in the Kidney Proximal Tubules and Reversibly Accumulate Within the Nuclei. The nephron distribution of the construct was evaluated as a function of time from 1 min to 7 d by IF, IHC, and NIR imaging (Fig. 3 and Fig. S4). A strong correlation between the IHC and IF results was seen, although IHC found higher background staining, whereas IF revealed a more detailed structure. In the first minute postinjection, SWCNTs appeared in the glomerular capillaries, as well as in the Bowman capsule and the tubular system. No significant signal was visualized in the peritubular capillaries or the basolateral compartments, suggesting mainly a first-pass filtration clearance. Of note, the highest IF and IHC signals were associated with the luminal side of proximal tubular cells (brush border) rather than distal tubules and collecting ducts. The signal remained in this location and increased in intensity at 3 and 5 min. At 20 min, the signal was associated not only with the brush border, but also with the cytoplasm of proximal tubular cells (punctate pattern). Perinuclear and nuclear compartments also were stained in some of the proximal tubular cells. The nuclear/perinuclear staining intensity increased at 60 min (Fig. 4*A*) and 180 min (Fig. 3), whereas the cytoplasmic signal diminished. At 24 h, most of the signal cleared from the nuclei and again appeared to be cytoplasmic (punctate pattern). After 7 d, the construct staining was very weak, and only a few tubules were stained. The PK of AF488 dye alone was acquired at 1 and 60 min as a control (Fig. S4). The AF488 dye was filtered rapidly and completely, with staining apparent only in the tubules in the first minute and no sign of retention at 60 min. An in vitro time course study using polarized human proximal renal tubular cells (HK-2 cells) (Fig. 4 *C*–*H* and Fig. S5) revealed a similar accumulation of construct in these cells, again with preferential uptake from the luminal side (Fig. 4*I*).

Mathematical Modeling Explains How These High–Aspect Ratio Molecules Align with Flow and Access the Glomerular Pores, Allowing Rapid Clearance Compared with Globular Molecules. The lengths of the SWCNTs (based on TEM data) used were 100–500 nm, and any individualized construct greatly exceeded the apparent diameter of the glomerular capillary pores (~10 nm). Accordingly, to pass through the capillary wall at an appreciable rate during filtration, the CNTs must be highly oriented, with the long

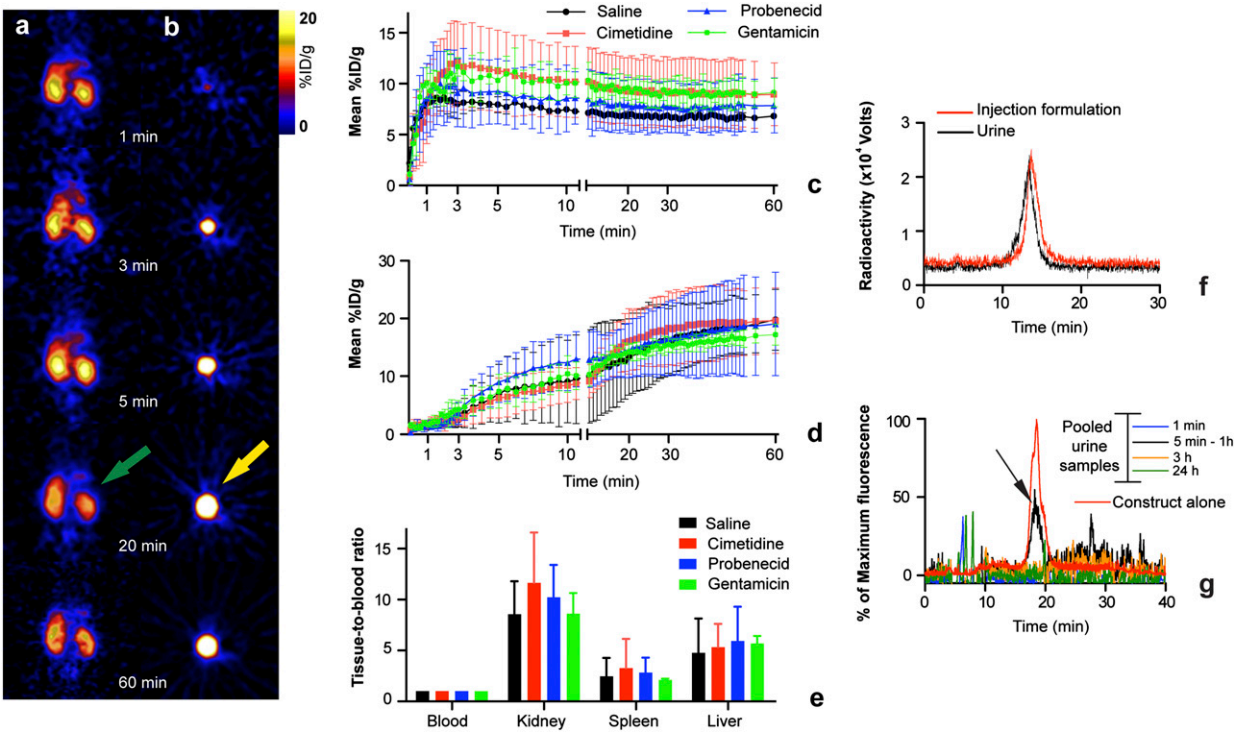

Fig. 2. Renal clearance data for SWCNT-[([^{86}Y]DOTA)(AF488)(AF680)] in mice. (*A* and *B*) Dynamic PET images of a representative animal showing rapid renal clearance in kidney coronal sections (green arrow) (*A*) and transverse bladder sections (yellow arrow) (*B*) at different time points. (*C* and *D*) Time activity curve % ID/g data (mean ± SD) obtained from VOI analysis of PET images of the kidneys (*C*) and bladders (*D*) of mice in the three groups receiving the inhibitors of active secretion and a saline control group. The 3 min kidney accumulation values (mean ± SD) were saline, 8.0 ± 1.4%ID/g; cimetidine, 12.1 ± 3.9%ID/g; probenecid, 9.1 ± 3.3%ID/g; and gentamicin, 11.6 ± 0.9%ID/g. Bladder accumulated activity at 20 min were saline, 13.3 ± 6.5%ID/g; cimetidine, 16.0 ± 5.6%ID/g; probenecid, 14.4 ± 4.6%ID/g; and gentamicin, 14.2 ± 1.2%ID/g. (*E*) Tissue-to-blood data from the tissue harvest data of the mice in the active secretion study. (*F*) Radioactivity chromatograph of urine sample (black trace) from a mouse that received SWCNT-[([^{86}Y]DOTA)(AF488)(AF680)] overlaid with a sample of the injected construct (red trace). (*G*) Fluorescence chromatograph (black trace) of urine samples collected at 1 min, 5–60 min, 3 h, and 24 h from mice given SWCNT-[(DOTA)(AF488)(AF680)] overlaid with a sample of the injected construct (red trace).

axis directed toward the openings, as shown in Fig. 5*A*. As with the flow of a dilute suspension of fibers toward an orifice, the tendency of the velocity field to create such an end-on orientation will be opposed by Brownian motion; that is, random rotation of the fibers due to thermal motion tends to preclude any preferred orientation. The competition between these processes is embodied in the ratio $\gamma/D_{\rm rot}$, where γ is the rate of strain in the fluid and $D_{\rm rot}$ is the rotational diffusivity of a fiber or molecule. Large values of this ratio (compared with unity) indicate a strong tendency for flow-induced orientation, and small values suggest nearly random orientations (20).

If the mean fluid velocity at an orifice is u and the radius of the opening is r, then a suitable measure of the local rate of strain is $\gamma = 4u/r$ (20). For a rigid rod of length L and diameter d, such that L/d is large, the rotational diffusivity is described by the following equation:

$$D_{rot} = \frac{3K_BT}{\pi\mu L^3}\ln\left(\frac{L}{d}\right), \qquad [1]$$

where K_B is Boltzmann's constant, T is temperature, and μ is the viscosity of the solvent (21). Using $u = 2 \times 10^{-5}$ m/s (average

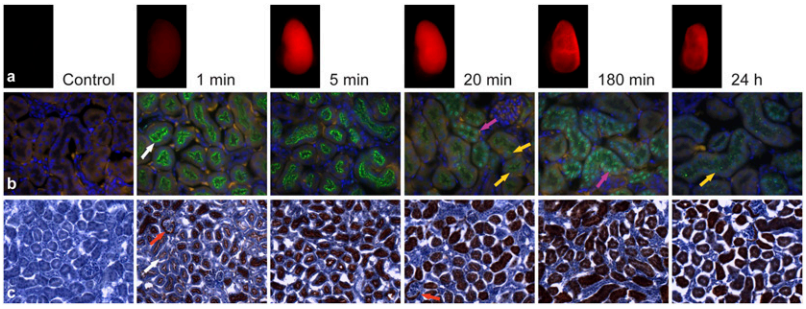

Fig. 3. NIR images of harvested kidneys and corresponding IF and IHC microscopic sections of the kidneys of mice injected with SWCNT-[(DOTA)(AF488)(AF680)]. Time course imaging of kidneys of animals injected with SWCNT-[(DOTA)(AF488)(AF680)] using NIR imaging (*A*), IF (composite image: DAPI+AF488+TRITC) (*B*), and IHC (*C*). Reported is construct accumulation in the proximal tubule brush border (white arrows) and glomerulus (red arrows) in the first minutes and progressively cytoplasmic (yellow arrows) and nuclear accumulation (magenta arrows) in tubular cells.

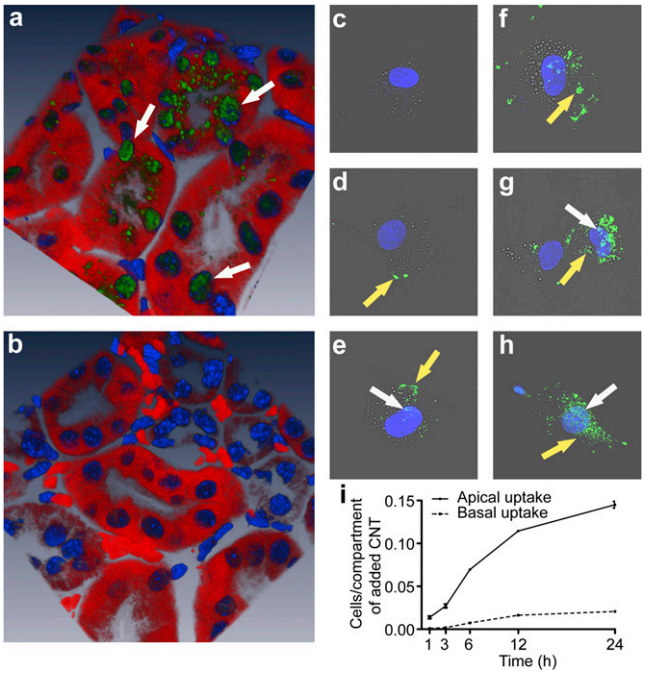

Fig. 4. In vivo and in vitro kidney cell uptake of SWCNT-[(DOTA)(AF488)(AF680)]. (*A* and *B*) Confocal microscopic 3D-reconstructed IF image of the kidney cortex in mice injected with SWCNT-[(DOTA)(AF488)(AF680)] at 1 h postadministration, showing both punctate cytoplasmic and nuclear accumulation (*A*), and control (not-injected) mice (*B*). (*C–H*) Composite [AF488, DAPI, and differential interference contrast (DIC)] confocal images of HK-2 cells not exposed (*C*) and exposed to SWCNT-[(DOTA)(AF488)(AF680)] for 30 min (*D*), 60 min (*E*), 6 h (*F*), 12 h (*G*), and 24 h (*H*). Progressive accumulation of the construct in the cytoplasm (yellow arrow) and nuclei (white arrow). (*I*) Differential uptake of SWCNT-[([^{111}In]DOTA)(AF488)(AF680)] by polarized HK-2 cells exposed on either the apical (brush border) side or the basal side using the Transwell chamber. Construct uptake was higher from the apical side than from the basolateral side ($P < 0.05$).

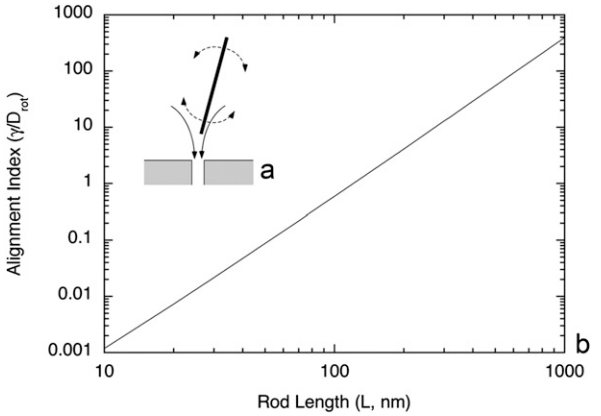

Fig. 5. Mathematical modeling of the rotational diffusivity showed the tendency of flow to orient SWCNT of this size to allow clearance via the glomerular pores. (*A*) Schematic of a long, rod-like molecule approaching the entrance of a pore in a filtration process. The converging flow (solid curves) tends to align the major axis of the rod with the pore. This is opposed by rotational diffusion (dashed curves), which tends to randomize the rod orientations. If the rod length greatly exceeds the pore diameter (as shown), entry into the pore is probable only if the rotational Brownian motion is sufficiently weak to permit a high degree of alignment. (*B*) Predicted effect of molecular length on the tendency of a rod-like molecule to align end-on at a glomerular pore. The rod diameter is assumed to be 1 nm, and the other inputs are as described in the text. Values of γ/D_{rot} much larger than unity, as for the SWCNT studied, suggest high degrees of alignment and a greatly increased probability of entering pores in the capillary wall.

velocity at a fenestral opening) and $r = 5 \times 10^{-9}$ m (22), a representative rate of strain for fluid entering a glomerular pore is $\gamma = 1.6 \times 10^{4}$ s^{-1}. With $K_B = 1.38 \times 10^{-23}$ J/K, $T = 310$ K, $\mu = 7 \times 10^{-4}$ Pa·s, $d = 1$ nm, and average $L = 200$–300 nm, the rotational diffusivity of a SWCNT is estimated as $D_{rot} = 1.1 \times 10^{3}$ s^{-1}. Thus, $\gamma/D_{rot} \cong 9$–15. (An average length range of 200–300 nm was used for this calculation based on TEM and DLS data.)

Discussion

In this article, we have described how large molecules with high MW and high aspect ratio, such as CNTs, have unique properties in terms of renal clearance. These molecules' unique PK profile makes them an appealing paradigm to better understand kidney glomerular physiology and suggest the potential design features (e.g., shape and aspect ratio) of novel constructs with improved clearance properties.

The glomerulus acts as a highly selective filter consisting of the fenestrated endothelium, the glomerular basement membrane, and the interdigitated foot processes of podocytes. In addition to the heteroporous structure (i.e., many small and a few large pores) of the glomerular filter (23), there are also filtration slits bounded by podocytes with zipper-like structures and openings postulated to have dimensions of 4 nm × 14 nm, corresponding to a slit half-width of 2 nm (24).

The appearance of radioactivity in the bladder within the first minute postinjection strongly suggests a rapid translocation of SWCNTs from the vascular compartment to the urine compartment through glomerular filtration. This finding was surprising, given that predicting the transglomerular passage of a solute entails consideration of the molecular size, net charge, and configuration, and in practice, albumin-sized globular proteins (~50 kDa) typically are not filtered (24, 25). Albumin has a Stokes-Einstein radius of 3.5 nm and is associated with a very low sieving coefficient ($\Theta = 0.0021$) (26). However, elongated molecules, such as bikunin and hyaluronan, behave differently, resulting in >100-fold higher sieving coefficients than albumin, despite similar MWs and charges. Moreover, the fact that the threshold for the glomerular filtration of polymers is in the range of 30–50 kDa and also depends on charge, molecular conformation, and deformability must be taken into account (24, 27). Because of its high aspect ratio ($d \sim 1$ nm, $100 \leq L \leq 500$ nm), negative charge, and high MW (150–750 kDa), our construct largely exceeds the structural sizes of glomerular pores (at least in the longitudinal dimension), as well as the sizes of other molecules used to investigate glomerular filtration. Despite these features, however, we observed the renal elimination of ~65% of the recovered construct, with ~15% of the construct undergoing passive reabsorption within the tubules at 20 min postinjection.

Lacerda et al. (11) reported TEM evidence of several MWCNT molecules translocating via their transverse dimension directly into the Bowman capsule. This same group also reported a dynamic SPECT study to image the rapid clearance of their radiolabeled MWCNTs in a mouse model into the urine (10). In the present work, we investigated in detail the kinetics of glomerular filtration with well-characterized, multifunctional probes, as well as the contribution of secretion and reabsorption to the overall clearance mechanism.

In addition, we have provided a theoretical model suggesting that the flow is sufficiently strong to steer the CNTs into the pores, which provides a physical explanation for their rapid clearance into urine. As shown in Fig. 5*B*, if L were a factor of 10 smaller (30 nm), then D_{rot} would increase by three orders of magnitude, and the balance would shift toward no preferred orientation. Further reducing L to 10 nm (roughly the length of an albumin molecule) would further decrease the tendency

toward flow-induced orientation by another order of magnitude. Thus, this mechanism for enhancing the passage of large molecules appears to be unique to entities with dimensions like those of the SWCNTs studied.

We used DLS measurements as well as TEM to characterize the lengths of our SWCNTs. TEM evaluates a small amount of the CNT batch (28), and DLS measurements of cylindrical CNTs rely on spherical geometric assumptions to yield a value for the size. The DLS data provide an average hydrodynamic radius (R_h) using this spherical assumption. We then assume a rod shape to relate R_h to the radius of gyration (R_g). The R_g for rods depends on the aspect ratio (i.e., length/diameter ratio). Our measured average value ranges of L ~200–300 nm reflect the measured lengths of the SWCNTs based on both methods. TEM images (Fig. S1) showed microscopic images of the SWCNTs with sizes consistent with the DLS predictions.

Our previous PK report on analogous SWCNT constructs demonstrated a slower beta clearance phase from the kidney that can now be explained as the fraction of construct that was transiently taken into the tubule cells by reabsorption and then cleared (7). Presumably, the reabsorbed construct was processed in the tubules and then released back to the blood, which also demonstrated a slower beta clearance phase (8), for filtration.

The PK profile of different CNT constructs varies depending on the chemical composition. Pristine SWCNTs have shown significant reticuloendothelial system (RES) tropism, attributable to the lipophilicity of the carbon atoms (29); noncovalently PEG-functionalized SWCNTs were found to have long blood circulation with RES uptake (14); and covalently functionalized SWCNTs and MWCNTs demonstrated renal clearance with limited RES uptake (5–12). Pristine CNTs, dispersed with surfactants, favor liver accumulation and hepatobiliary excretion over kidney accumulation and renal excretion, whereas covalently modified CNTs favor the converse. The constructs in the present study did accumulate about 7% of the injected dose in the liver. The PK profiles of these materials were complex, but they can be manipulated through the construct design.

Finally, we and others did not observe any glomerular or tubular cell toxicity or modification of the nephron structure or any chronic toxicity with functionalized CNTs (6–12, 30–32). The importance of understanding the PK and toxicity of these novel CNT materials is crucial to the development of medically useful agents (33). Of course, the PK profile may vary depending on the stoichiometry and identity of the moieties attached to the CNT. Clearly, the results reported herein demonstrate the surprising ability of the mammalian kidney to immediately and efficiently eliminate large, soluble, covalently functionalized CNT nanomaterials intact through glomerular filtration. The tubular reabsorption component of the mechanism seemed to be transient, and the absorbed CNTs were released to presumably undergo further rounds of elimination in the slower beta clearance phase (see blood and tissue PK in refs. 8 and 7, respectively). Reversible accumulation of PEGylated SWCNTs in mammalian cell nuclei has been reported only in vitro (34) and is an area of interest that merits further investigation. We have described progressive directional accumulation of the construct in polarized HK-2 cells in vitro as well as in vivo.

In conclusion, the kidney was able to rapidly and effectively eliminate xenobiotics from the blood compartment without concomitant degradation, which is the most desired clearance route for imaging and therapeutic constructs. Surprisingly, this large molecule, with an aspect ratio ranging from 100:1 to 500:1, was cleared similarly to a small molecule. Thus, a better understanding of the biophysics of novel materials within the glomerular filter will help further define the design criteria for new, potentially medicinally useful constructs.

Materials and Methods

Synthesis and Characterization of the SWCNT-[(DOTA)(AF488)(AF680)] Construct. Raw HiPCO SWCNTs (Unidym) were not acid-treated or sonicated, but were covalently amine-functionalized as described previously (2–4, 6–9). The SWCNT-NH_2 product was purified from carbonaceous impurities using C18 Sep-Pak cartridges (Waters) and analyzed by HPLC, Raman spectroscopy, and TEM (Fig. 1 and *SI Materials and Methods*). The amine loading was determined using the Sarin assay, and TEM and Raman spectroscopy were performed as described previously (7–9). Details of SWCNT functionalization with the different fluorophores and radiolabeling procedures are provided in *SI Materials and Methods*.

Size and Charge Characterization. DLS and ζ-potential measurements were performed using a Zetasizer Nano ZS system equipped with a narrow bandwidth filter (Malvern Instruments). The SWCNT construct was diluted 1:10 in 10 mM Hepes buffer (pH 7.2), and measurements were carried out in triplicate. The average size of the SWCNTs [$2 \times R_h$ (radius of hydration)] was obtained with the nonnegative least squares fitting algorithm provided with the DLS software, using an assumed spherical geometry. The R_h value was converted to the radius of gyration (R_g) for a cylinder ($R_g = 1.732 \times R_h$). The approximate length of the SWCNTs was calculated using the relation $R_g = (L^2/12 + R^2/2)^{1/2}$, where L is length and R is the radius of a cylinder. The ζ-potential was calculated via the Henry equation using the Smoluchowski approximation, (K_a) = 1.5 (35).

Dynamic PET Imaging. Dynamic PET imaging was performed with the Focus 120 micro-PET system (CTI Molecular Imaging). Mice (males, NCr/nu/nu; Taconic) were maintained under 2% isoflurane/oxygen anesthesia during the scanning. One-hour list-mode acquisitions were initiated at the time of i.v. injection of 0.008 mg per mouse [initially 2.78 MBq (0.075 mCi)] of CNT-[([^{86}Y]DOTA)(AF488)(AF680)] via a 27 G tail vein catheter (Visual Sonics) placed in the lateral tail vein (*SI Materials and Methods*). For all in vivo experiments, housing and care were provided in accordance with the Animal Welfare Act and the Guide for the Care and Use of Laboratory Animals. The animal protocols were approved by MSKCC's Institutional Animal Care and Use Committee.

Organic Cationic Transport, Organic Anionic Transport, and Megalin Receptor Competition Studies. Fifteen mice (males, NCr/nu/nu) were randomly divided into four groups. Group I ($n = 4$) received an i.p. injection of normal saline, group II ($n = 4$) received an i.p. injection of cimetidine 100 mg/kg, group III ($n = 4$) received an i.p. injection of probenecid 20 mg/kg, and group IV ($n = 3$) received an i.p. injection of gentamicin 40 mg/kg (17–19). Each competitive inhibitor and the saline control were injected in a volume of 0.4 mL at ≈0.5 h before the start of SWCNT construct administration and imaging.

HPLC Analysis of Urine Samples. In one experiment, eight mice (males, NCr/nu/nu) that received 0.01 mg of SWCNT-[(DOTA)(AF488)(AF680)] in 0.10 mL via retroorbital sinus i.v. injection, and one mouse received no construct and served as a control. Mice were killed at 1, 3, 5, 20, 60, and 180 min, 24 h, and 7 d, after which the kidneys were harvested for NIR, IHC, and IF analyses and the urine was collected for HPLC analysis. HPLC analysis (method II; *SI Materials and Methods*) was performed using the AF680 NIR fluorescence signal to follow the construct. An aliquot of the construct and a sample of urine from an untreated mouse served as controls. Data were normalized to a percentage of maximum fluorescence for each run, and the background fluorescence from the untreated mouse urine was subtracted from each chromatograph.

Urine was harvested after the mice were euthanized in accordance with MSKCC's Institutional Animal Care and Use Committee protocol. The bladder was exposed by incision, and the urine was collected with a sterile 1-mL syringe (before any other tissue or blood harvesting was performed) and transferred to a tared 12 × 75 mm test tube, capped, and weighed.

In a second experiment, urine samples from the 15 mice in the four groups that underwent PET imaging were collected immediately after imaging (1 h postinjection of 0.008 mg of SWCNT-[([^{86}Y]DOTA)(AF488)(AF680)]). HPLC analysis (method I; *SI Materials and Methods*) was performed using the radioactivity signal to follow the construct. An aliquot of the construct served as a control.

Tissue Harvest for γ-Counting. After the dynamic PET imaging studies of the 15 mice to investigate biodistribution, clearance, and the effect of competitive inhibition of the active secretion transporters, each animal was killed by CO_2 aspiration. Tissue samples (blood, kidney, liver, and spleen) and urine were harvested, weighed, and counted using a γ-counter (Packard) with a

315- to 435-keV energy window. Standards of the injected formulation were counted to determine the percentage of injected dose per gram (%ID/g).

Tissue Harvest for IHC and IF Time Course Microscopy. Eight mice (males, NCr/nu/nu) received 0.01 mg of SWCNT-[(DOTA)(AF488)(AF680)] in 0.10 mL via retroorbital sinus i.v. injection, and one mouse received no construct and served as a control. Mice were killed at 1, 3, 5, 20, 60, 180 min, 24 h, and 7 d, after which the kidneys were harvested for IHC and IF analyses and the urine was collected for HPLC analysis. Kidneys were harvested, washed in ice-cold PBS, and fixed for 24 h in 4% paraformaldehyde, embedded in OCT, frozen at −80 °C, and cryosectioned to obtain 0.010-mm-thick samples. IHC and IF staining were performed as described in *SI Materials and Methods*.

NIR Fluorescence Imaging of the Construct in Kidney Samples ex Vivo. The NIR fluorescence signal of the SWCNT-[(DOTA)(AF488)(AF680)] construct was imaged in the kidneys after tissue harvest for the IHC and IF time course microscopy study. The kidneys were imaged with the Maestro Imaging System (CRi) using the yellow filter [excitation, 595 nm (range, 576–671 nm); emission, 635 nm, long-pass; acquisition: 630–800 nm in 10 steps]. We performed spectral separation of the fluorescence of the injected compound from the kidney parenchyma autofluorescence and from the background. We report kidney images in which only the construct NIR signal is visible.

HK-2 Cells. HK-2 cells derived from normal kidney were obtained from American Type Culture Collection. HK-2 cells were cultured in Keratinocyte Serum-Free Medium (Invitrogen) containing 0.05 g/L of bovine pituitary extract and 5 ng/mL of EGF at 37 °C and 5% CO_2. The HK-2 cells were seeded on 24-mm-diameter polyester filters (1×10^5 cells/well) with a pore size of 0.4 μm (Transwell Clears; Corning-Costar) (see Fig. S6 for experimental design). The cells were cultured for 7 d to the allow cells to attach and polarize (36).

Data Analysis. Three-dimensional VOI analysis on PET images was performed with AsiPRO VM 5.0 software (Concorde Microsystems). TEM image analysis was performed using ImageJ software (http://rsb.info.nih.gov/ij/). Wide-field and confocal microscopy images were evaluated using ImageJ, AxioVision LE (Zeiss), and Amira 4.1 (Visage Imaging) software. Statistical data were evaluated using Graphpad Prism 5.0 (Graphpad Software). NIR images were analyzed using Maestro 2.6 software (CRi). Statistical comparisons between two experimental groups were performed using *t* tests (unpaired comparisons); comparison of multiple groups was performed with one-way ANOVA using Bonferroni's multiple comparison post hoc analysis. All statistical comparisons were two-sided, and the level of statistical significance was set at $P < 0.05$.

ACKNOWLEDGMENTS. We acknowledge the expert advice and technical assistance of Dr. Pat Zanzonico, Dr. Jelena Vider, Mesruh Turkekul, Dr. Afsar Barlas, Valerie Longo, Larissa Shenker, and Dr. Surya Seshan. We also thank Dr. Hongjie Dai for the helpful discussions of this work. This work was supported by the National Institutes of Health (Medical Scientist Training Program [MSTP] Grant GM07739 and Grants R21 CA128406, R01 CA55399, R25T CA096945, R24 CA83084, P30 CA08748, and P01 CA33049), the Memorial Sloan-Kettering Cancer Center Brain Tumor Center, the Memorial Sloan-Kettering Cancer Center Experimental Therapeutics Center, and the US Department of Energy, Office of Science Biological and Environmental Research (BER) (Award DE-SC0002456).

1. Kostarelos K, Bianco A, Prato M (2009) Promises, facts and challenges for carbon nanotubes in imaging and therapeutics. *Nat Nanotechnol* 4:627–633.
2. Georgakilas V, et al. (2002) Amino acid functionalisation of water-soluble carbon nanotubes. *Chem Commun (Camb)* 5:3050–3051.
3. Tasis D, Tagmatarchis N, Bianco A, Prato M (2006) Chemistry of carbon nanotubes. *Chem Rev* 106:1105–1136.
4. Singh P, et al. (2009) Organic functionalisation and characterisation of single-walled carbon nanotubes. *Chem Soc Rev* 38:2214–2230.
5. Wang H, et al. (2004) Biodistribution of carbon single-wall carbon nanotubes in mice. *J Nanosci Nanotechnol* 4:1019–1024.
6. Singh R, et al. (2006) Tissue biodistribution and blood clearance rates of intravenously administered carbon nanotube radiotracers. *Proc Natl Acad Sci USA* 103:3357–3362.
7. McDevitt MR, et al. (2007) Tumor targeting with antibody-functionalized, radiolabeled carbon nanotubes. *J Nucl Med* 48:1180–1189.
8. McDevitt MR, et al. (2007) PET imaging of soluble yttrium-86–labeled carbon nanotubes in mice. *PLoS ONE* 2:e907.
9. Villa CH, et al. (2008) Synthesis and biodistribution of oligonucleotide-functionalized, tumor-targetable carbon nanotubes. *Nano Lett* 8:4221–4228.
10. Lacerda L, Soundararajan A, Singh R (2008) Dynamic imaging of functionalized multi-walled carbon nanotube systemic circulation and urinary excretion. *Adv Mater* 20: 225–230.
11. Lacerda L, et al. (2008) Carbon nanotube shape and individualization critical for renal excretion. *Small* 4:1130–1132.
12. Lacerda L, et al. (2008) Tissue histology and physiology following intravenous administration of different types of functionalized multiwalled carbon nanotubes. *Nanomedicine (Lond)* 3:149–161.
13. Longmire M, Choyke PL, Kobayashi H (2008) Clearance properties of nano-sized particles and molecules as imaging agents: Considerations and caveats. *Nanomedicine (Lond)* 3:703–717.
14. Liu Z, et al. (2008) Circulation and long-term fate of functionalized, biocompatible single-walled carbon nanotubes in mice probed by Raman spectroscopy. *Proc Natl Acad Sci USA* 105:1410–1415.
15. Birkett D (1992) Clearance of drugs by the kidneys. *Aust Prescriber* 15:16–19.
16. Liu Z, Tabakman S, Welsher K, Dai H (2009) Carbon nanotubes in biology and medicine: In vitro and in vivo detection, imaging, and drug delivery. *Nano Res* 2: 85–120.
17. Hörbelt M, et al. (2007) Organic cation transport in the rat kidney in vivo visualized by time-resolved two-photon microscopy. *Kidney Int* 72:422–429.
18. Stahl AR, et al. (2007) Renal accumulation of [^{111}In]DOTATOC in rats: Influence of inhibitors of the organic ion transport and diuretics. *Eur J Nucl Med Mol Imaging* 34: 2129–2134.
19. Schmitz C, et al. (2002) Megalin deficiency offers protection from renal aminoglycoside accumulation. *J Biol Chem* 277:618–622.
20. Mongruel A, Cloitre M (2003) Axisymmetric orifice flow for measuring the elongational viscosity of semi-rigid polymer solutions. *J Non-Newt Fluid Mech* 110:27–43.
21. Broersma S (1960) Rotational diffusion constant of a cylindrical particle. *J Chem Phys* 32:1626–1631.
22. Deen WM, Lazzara MJ, Myers BD (2001) Structural determinants of glomerular permeability. *Am J Physiol Renal Physiol* 281:F579–F596.
23. Deen WM, Bridges CR, Brenner BM, Myers BD (1985) Heteroporous model of glomerular size selectivity: Application to normal and nephrotic humans. *Am J Physiol* 249:F374–F389.
24. Haraldsson B, Nyström J, Deen WM (2008) Properties of the glomerular barrier and mechanisms of proteinuria. *Physiol Rev* 88:451–487.
25. Ohlson M, et al. (2001) Effects of filtration rate on the glomerular barrier and clearance of four differently shaped molecules. *Am J Physiol Renal Physiol* 281: F103–F113.
26. Lindström KE, Johnsson E, Haraldsson B (1998) Glomerular charge selectivity for proteins larger than serum albumin as revealed by lactate dehydrogenase isoforms. *Acta Physiol Scand* 162:481–488.
27. Fox ME, Szoka FC, Fréchet JMJ (2009) Soluble polymer carriers for the treatment of cancer: The importance of molecular architecture. *Acc Chem Res* 42:1141–1151.
28. Itkis ME, Perea DE, Jung R, Niyogi S, Haddon RC (2005) Comparison of analytical techniques for purity evaluation of single-walled carbon nanotubes. *J Am Chem Soc* 127:3439–3448.
29. Cherukuri P, et al. (2006) Mammalian pharmacokinetics of carbon nanotubes using intrinsic near-infrared fluorescence. *Proc Natl Acad Sci USA* 103:18882–18886.
30. Schipper ML, et al. (2008) A pilot toxicology study of single-walled carbon nanotubes in a small sample of mice. *Nat Nanotechnol* 3:216–221.
31. Sayes CM, et al. (2006) Functionalization density dependence of single-walled carbon nanotubes cytotoxicity in vitro. *Toxicol Lett* 161:135–142.
32. Dumortier H, et al. (2006) Functionalized carbon nanotubes are non-cytotoxic and preserve the functionality of primary immune cells. *Nano Lett* 6:1522–1528.
33. Kostarelos K (2008) The long and short of carbon nanotube toxicity. *Nat Biotechnol* 26:774–776.
34. Cheng J, et al. (2008) Reversible accumulation of PEGylated single-walled carbon nanotubes in the mammalian nucleus. *ACS Nano* 2:2085–2094.
35. Milton K (1997) *Scattering of Light and Other Electromagnetic Radiation* (Academic Press, New York).
36. Yuan ZX, et al. (2009) Specific renal uptake of randomly 50% N-acetylated low molecular weight chitosan. *Mol Pharm* 6:305–314.